High pressure behavior, transformation and crystal structure of synthetic iron-free pigeonite

Fabrizio Nestola,[1] Mario Tribaudino,[1,*] and Tiziana Boffa Ballaran[2]

[1]Dipartimento di Scienze Mineralogiche e Petrologiche, Via Valperga Caluso 35, I-10125, Torino, Italy
[2]Bayerisches Geoinstitut, Universität Bayreuth, 95440 Bayreuth, Germany

Abstract

A single-crystal high pressure X-ray investigation was performed up to $P = 6.5$ GPa on a synthetic clinopyroxene of composition $Ca_{0.15(1)}Mg_{1.85(1)}Si_{2.00(1)}O_6$ [$Di_{15}En_{85}$, unit-cell parameters at room pressure: $a = 9.6525(6)$Å, $b = 8.8461(2)$Å, $c = 5.2036(5)$Å, $\beta = 108.370(5)°$, $V = 421.68(4)$Å^3]. A first order $P2_1/c$-$C2/c$ displacive phase transition was found at $P = 5.1$ GPa; the transition was revealed by the disappearance of the *b* reflections ($h + k = $ odd) and by sharp changes in the unit-cell parameters. Reversals through the transformation show that, if present, hysteresis is smaller than 0.1 GPa. The volume variation has been described by a third-order Birch-Murnaghan equation of state with $V_0 = 421.68(8)$ Å^3, $K_{T0} = 102(2)$ GPa, and $K' = 8(1)$ for the low-symmetry phase ($P2_1/c$) and with $V_0 = 411.06(3)$ Å^3 and $K_{T0} = 108(2)$ GPa for the high-symmetry phase ($C2/c$), with K' fixed to the value obtained for the low-symmetry form. The axial compressibility shows the following scheme: $\beta_b > \beta_a \cong \beta_c > \beta_{a\sin\beta}$ for both phases. In comparison with pure clinoenstatite, $Di_{15}En_{85}$ shows a similar step in unit-cell parameters at the transition, the disappearence of hysteresis and a decrease of transition pressure and of bulk modulus.

Full intensity data sets were collected at room pressure, 2.6 and 4.5 GPa for the $P2_1/c$ phase and at $P = 6.2$ GPa for the $C2/c$ phase. A slight increase of the intensity of $h + k$ odd reflections and of the difference in the A and B chain kinking angles were observed. A comparison of the structural behavior of the $P2_1/c$ phase at high temperature and high pressure shows opposite behavior for M2-O bond lengths and O3-O3-O3 kinking angle.

Introduction

Several recent studies have been devoted to the investigation of the structural and thermodynamic features of the $P2_1/c$-$C2/c$ phase transition in pyroxenes at high pressure. This transition was first found by Angel et al. (1992) for clinoenstatite and subsequently reported for clinoferrosilite (Hugh-Jones et al. 1994), for intermediate clinopyroxenes along the join En-Fs (Ross and Reynard 1999), for Cr^{3+}-clinopyroxenes and kanoite (Arlt et al. 1998; Arlt et al. 2000), and for spodumene, LiScSi$_2$O$_6$, and Zn$_2$Si$_2$O$_6$ pyroxenes (Arlt and Angel 2000). In all these studies, the transition was found to be first order, with little or no hysteresis apart from clinoenstatite and Mg-rich samples belonging to the En-Fs join (Angel and Hugh-Jones 1994; Ross and Reynard 1999; Shinmei et al. 1999). In natural clinoenstatite exsolved in diopside, the same transition probably occurred during decompression in rocks that underwent ultra-high-pressure metamorphism (Bozhilov et al. 1999; Arlt et al. 2000). The transition pressure (P_c) changes with composition, depending on the average radius of the cation in the M2 site (Arlt et al. 2000) and on crystal field stabilization energy (Arlt et al. 1998; Ross and Sowerby 1999). The most important cation substitutions in natural pyroxenes are those of Fe and Ca into the MgSiO$_3$ end-member. Iron substitution induces a decrease in P_c and a disappearance of hysteresis (Hugh-Jones et al. 1994; Ross and Reynard 1999). Calcium substitution also may have an effect on the transition character as recent results on Ca-bearing clinopyroxenes (Tribaudino et al. 2001) show deviations from classic first-order behavior. In these samples, mottled textures preliminary to exsolution and small-sized antiphase domains have been observed (Tribaudino 2000; Pasqual et al. 2000). Such microtextures add a strain component that may interact with the spontaneous strain at the transition.

In this study, the high-pressure $P2_1/c$-$C2/c$ phase transition has been investigated in a synthetic sample with composition $Ca_{0.15}Mg_{1.85}Si_2O_6$, free of microtextures, in order to clarify the effect of Ca on the transition pressure and on the thermodynamic behavior without the effect of coexisting microtextural inhomogeneities. This synthetic sample comes from the same run used for a previous high-temperature investigation (Tribaudino et al. 2002), and will enable a comparison of the structural changes induced by the HP and HT transition on the same sample and of the pre-transition features for the $P2_1/c$ phase.

Experimental methods

A single-phase clinopyroxene assemblage of composition $Ca_{0.15}Mg_{1.85}Si_2O_6$ ($Di_{15}En_{85}$) was synthesized from gel at room pressure and $T = 1370$ °C for 624 h; single crystals were chosen from such run for this work and for high-temperature investigations on the basis of their sharp optical extinction; the lack of twinning was checked by preliminary single-crystal X-ray analysis. The results of the sample characterization by powder X-ray diffraction (XRD), microprobe analysis, and transmission electron microscopy can be found in Tribaudino et al. (2002).

Crystals were loaded in a BGI design diamond-anvil cell (Allan et al. 1996), using a steel gasket and a 4:1 mixture of methanol:ethanol as pressure medium. A ruby chip for approximate pressure measurement and a quartz crystal as an internal diffraction pressure standard (Angel et al. 1997) also were loaded into the pres-

* E-mail: mario.tribaudino@unito.it

sure cell. Two crystals (sized respectively $175 \times 100 \times 70$ μm and $140 \times 110 \times 70$ μm, crystals x1 and x2) were investigated to determine the evolution of unit-cell parameters, owing to failure of one crystal during compression. A larger crystal ($220 \times 110 \times 90$ μm, x3) was used for structural determination.

Unit-cell parameters were determined by XRD using a HUBER four-circle diffractometer. Full details of the instrument and the peak-centering algorithms are provided by Angel et al. (2000). During the centering procedure, the effects of crystal offsets and diffractometer aberrations were eliminated from refined peak positions by the eight-position centering method of King and Finger (1979). Unconstrained unit-cell parameters were found to be within one estimated standard deviation of symmetry constrained unit-cell parameters. Unit-cell parameters obtained by vector-least-squares (Ralph and Finger 1982) are reported in Table 1. A set of $h + k$ odd reflections was measured at each pressure, before further compression to monitor the occurrence of the transition. The unit-cell parameters of the three crystals follow very closely the same trend, and therefore were used together in the following discussion.

Data for full structure determination were collected on a CAD4 diffractometer using monochromatic MoKα radiation. The data sets at room pressure, 4.5 and 6.2 GPa were measured during compression, that at 2.6 GPa during decompression. The intensities were measured by ω-scan, with 0.8° scan range and scan time up to 600 sec. Two sets of equivalent reflections were measured ($\pm h \pm k + l$), with $2 \leq 2\theta \leq 60°$. The program Win-IntegrStp (Angel 2003) was used to integrate the step-scan data. After correction for absorption by the crystal (μ= 12.618 cm^{-1}) with the program ABSORB (Angel personal communication, downloaded from http://www.crystal.vt.edu/crystal/) the data were reduced for structure factors and averaged in Laue group 2/m. Weighted structural refinements were done using SHELX-97 package (Sheldrik 1997); scattering factors were taken from the *International Tables for X-Ray Crystallography* (Wilson 1995). The refinement was performed in $P2_1/c$ for data collections at 0.0001, 2.6, and 4.5 GPa, starting from the coordinates of Di$_{15}$En$_{85}$ at room T as determined in Tribaudino and Nestola (2002), and in space group $C2/c$, starting from the coordinates of diopside (Bruno et al. 1982) at 6.2 GPa. Anisotropic refinement was allowed for the M2 site, constraining the coordinates to the same value and the occupancy of Ca and Mg in the M2 site [0.85 and 0.15 apfu. respectively, EDS analytical data (Tribaudino and Nestola 2002)]; M2 displacement ellipsoid was always positively definite. Anisotropic refinement for the M2 site was needed in order to describe the Ca and Mg site splitting in subsites, as found in Tribaudino and Nestola (2002). All the other atoms were refined isotropically. Unit-cell parameters, refinement results, atom coordinates, anisotropic and isotropic displacement parameters, selected bond lengths and angles are reported in Tables 2, 3, 4, and 5.

RESULTS

Phase transition

A sudden decrease in a, c, β, and V unit-cell parameters and a slight increase in b occur during compression at $P = 5.165(6)$ GPa (Fig. 1). At the same pressure, b-reflections ($h + k = $ odd), forbidden for the C-symmetry, disappear (Fig. 2). In agreement with previous observations on clinoenstatite (Angel et al. 1992),

we interpret these results as evidence of a $P2_1/c \rightarrow C2/c$ phase transition. At the transition, a discontinuity of about 2.6 vol% is present, showing that the transition is first order in character (Table 1). The volume decrease due to the transition is very similar for clinoenstatite (2.4%). Very slight decompression to $P = 5.084(6)$ GPa causes the reversal to $P2_1/c$ symmetry, indicating that hysteresis, if present, is less than 0.08 GPa.

A comparison with clinoenstatite can clarify the effect of Ca for Mg substitution on the transition. For clinoenstatite, a significant hysteresis was observed, varying from 1.7 GPa [be-
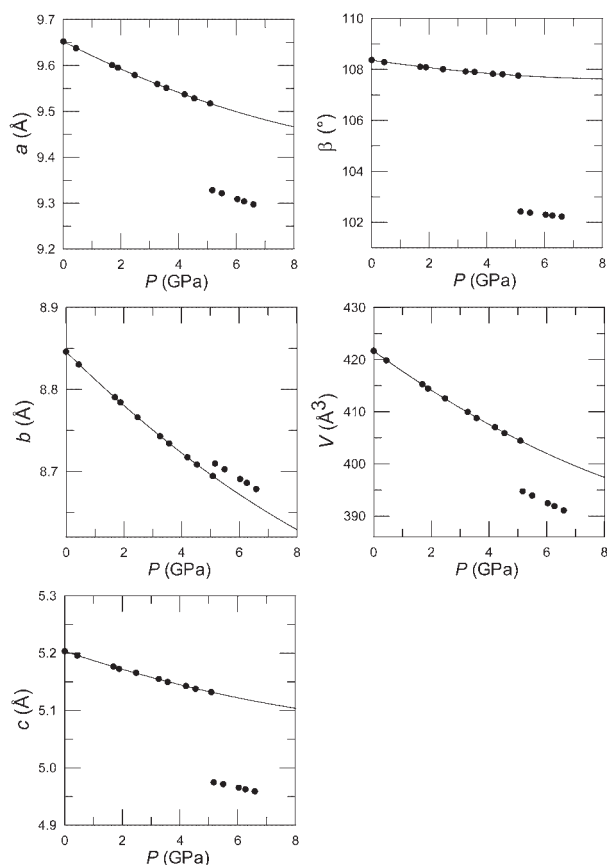

FIGURE 1. Unit-cell parameters vs P for the Di$_{15}$En$_{85}$ pyroxene. The $P2_1/c$ data were fitted by third-order Birch-Murnaghan (see text). The fit of β was recast from the fits on a and $a$sinβ. The size of the symbols is greater than the uncertainties.

TABLE 1. Unit-cell parameters vs. pressure in the Di$_{15}$En$_{85}$ pyroxene

P (GPa)	a (Å)	b (Å)	c (Å)	β (°)	V (Å³)
0.00010(1)	9.6525(6)	8.8461(2)	5.2036(5)	108.370(5)	421.68(4)
0.439(4)	9.6525(6)	8.8305(2)	5.1958(4)	108.280(5)	419.87(4)
1.689(5)	9.6011(5)	8.7907(2)	5.1768(4)	108.104(5)	415.29(3)
1.884(3)*	9.5954(3)	8.7843(1)	5.1727(4)	108.091(3)	414.45(3)
2.474(5)	9.5792(6)	8.7662(2)	5.1658(5)	108.010(6)	412.54(4)
3.258(5)	9.5597(6)	8.7430(2)	5.1550(5)	107.922(6)	409.95(4)
3.571(4)†	9.5510(4)	8.7342(1)	5.1496(3)	107.898(3)	408.79(3)
4.204(5)	9.5372(3)	8.7174(1)	5.1429(2)	107.828(3)	407.05(2)
4.538(5)†	9.5287(4)	8.7085(1)	5.1378(4)	107.812(4)	405.90(3)
5.084(6)	9.5174(4)	8.6944(2)	5.1322(3)	107.755(4)	404.46(3)
5.165(6)	9.3282(5)	8.7098(2)	4.9749(4)	102.427(5)	394.72(3)
5.492(4)	9.3215(5)	8.7027(2)	4.9716(4)	102.378(5)	393.94(3)
6.034(9)	9.3089(5)	8.6908(2)	4.9652(4)	102.297(5)	392.48(3)
6.265(7)	9.3040(6)	8.6861(2)	4.9626(5)	102.267(7)	391.90(4)
6.591(7)	9.2974(7)	8.6785(3)	4.9591(5)	102.226(8)	391.06(5)

Note: The datum at 5.084 GPa is the only one measured under decompression.
* Crystal x2.
† Crystal x3; when not indicated crystal x1.

TABLE 2. Unit-cell parameters and refinement data in the Di$_{15}$En$_{85}$ pyroxene

P (GPa)	0.0001	2.6	4.5	6.2
a (Å)	9.646(2)	9.546(2)	9.523(3)	9.291(2)
b (Å)	8.842(3)	8.732(3)	8.700(3)	8.679(3)
c (Å)	5.201(1)	5.149(1)	5.136(2)	4.963(1)
β (°)	108.35(2)	108.12(2)	107.80(2)	102.22(3)
Space group	$P2_1/c$	$P2_1/c$	$P2_1/c$	$C2/c$
Unique reflections	452	262	505	190
R_{int} (%)	6.0	5.2	6.6	3.3
$R_{4\sigma}$ (%)	5.0	5.8	5.2	3.4
R_{all} (%)	10.4	6.0	14.6	3.4
WR^2	14.1	13.0	14.0	8.0
GooF	1.11	1.13	0.92	1.26
NP	47	47	47	25

Note: NP = number of refined parameters.

TABLE 3. Fractional coordinates and displacement parameters in the Di$_{15}$En$_{85}$ pyroxene

P (GPa)	0.0	2.6	4.5	6.2
M2				
x	0.2553(4)	0.2562(7)	0.2562(4)	0.00000
y	0.0174(2)	0.0196(4)	0.0204(2)	0.2789(2)
z	0.2223(8)	0.2202(11)	0.2179(8)	0.25000
B$_{iso}$	1.7(2)	1.1(3)	1.2(1)	0.8(1)
U$_{11}$	0.0210(32)	0.0117(64)	0.0150(28)	0.0093(28)
U$_{22}$	0.0196(10)	0.0192(15)	0.0158(9)	0.0147(10)
U$_{33}$	0.0174(34)	0.0110(39)	0.0106(24)	0.0073(26)
U$_{12}$	0.0043(13)	0.0062(21)	0.0020(11)	0.00000
U$_{13}$	-0.0059(33)	0.0053(49)	-0.0012(28)	0.0017(26)
U$_{23}$	0.0042(12)	0.0040(18)	0.0052(12)	0.00000
M1				
x	0.2509(4)	0.2504(8)	0.2514(4)	0.00000
y	0.6538(2)	0.6552(4)	0.6559(2)	0.9065(2)
z	0.2217(8)	0.2216(12)	0.2192(8)	0.25000
B$_{iso}$	0.71(4)	0.75(6)	0.63(4)	0.55(4)
TA				
x	0.0424(4)	0.0422(6)	0.0416(3)	0.2976(2)
y	0.3409(2)	0.3415(3)	0.3424(2)	0.0918(1)
z	0.2873(7)	0.2862(9)	0.2866(6)	0.2139(5)
B$_{iso}$	0.62(4)	0.66(6)	0.54(4)	0.49(3)
TB				
x	0.5505(4)	0.5520(6)	0.5516(3)	
y	0.8378(2)	0.8387(3)	0.8381(2)	
z	0.2329(6)	0.2281(10)	0.2289(6)	
B$_{iso}$	0.65(4)	0.72(6)	0.57(4)	
O1A				
x	0.8671(8)	0.8656(16)	0.865(1)	0.1214(6)
y	0.3394(5)	0.3394(8)	0.3401(5)	0.0905(4)
z	0.178(2)	0.182(2)	0.182(2)	0.139(1)
B$_{iso}$	0.78(8)	0.79(1)	0.79(8)	0.63(6)
O2A				
x	0.1207(8)	0.1206(15)	0.1194(8)	0.3764(6)
y	0.5016(5)	0.5034(7)	0.5051(5)	0.2391(4)
z	0.324(2)	0.319(2)	0.318(2)	0.364(1)
B$_{iso}$	0.79(9)	0.7(1)	0.63(9)	0.83(7)
O3A				
x	0.1067(8)	0.1054(16)	0.1076(8)	0.3546(6)
y	0.2738(5)	0.2748(8)	0.2756(5)	0.0562(3)
z	0.600(2)	0.600(2)	0.603(2)	0.925(1)
B$_{iso}$	0.80(8)	1.0(1)	0.87(8)	0.69(6)
O1B				
x	0.3739(9)	0.3735(16)	0.3752(9)	
y	0.8398(5)	0.8383(8)	0.8389(5)	
z	0.128(2)	0.1265(24)	0.124(2)	
B$_{iso}$	0.79(7)	0.8(1)	0.71(8)	
O2B				
x	0.6307(8)	0.6293(15)	0.6321(8)	
y	0.9852(5)	0.9861(8)	0.9871(5)	
z	0.381(2)	0.382(2)	0.383(2)	
B$_{iso}$	1.26(8)	1.3(1)	1.03(5)	
O3B				
x	0.6047(9)	0.6062(16)	0.6086(9)	
y	0.7009(5)	0.6986(8)	0.6961(5)	
z	0.467(2)	0.458(2)	0.455(2)	
B$_{iso}$	1.03(8)	0.9(1)	0.87(5)	

TABLE 4. Selected bond lengths (Å) and angles (°) in P2$_1$/c structures of the Di$_{15}$En$_{85}$ pyroxene. Atom nomenclature as in Burnham et al. (1967)

P (GPa)	0.0001	2.6	4.5
TA-O1A	1.607(8)	1.600(15)	1.605(9)
TA-O2A	1.593(6)	1.584(9)	1.582(5)
TA-O3A	1.653(11)	1.634(17)	1.642(11)
TA-O3A	1.660(8)	1.646(12)	1.659(8)
<TA-O>	1.628	1.616	1.622
V$_{TA}$ (Å)^3	2.190	2.144	2.167
TQE$_{TA}$.	1.0081	1.0074	1.0085
TAV$_{TA}$	33.12	30.25	34.38
TB-O1B	1.618(9)	1.620(16)	1.588(5)
TB-O2B	1.585(5)	1.569(8)	1.599(9)
TB-O3B	1.661(14)	1.659(20)	1.670(6)
TB-O3B	1.679(7)	1.669(9)	1.681(13)
<TB-O>	1.636	1.629	1.634
V$_{TB}$ (Å^3)	2.232	2.206	2.230
TQE$_{TB}$	1.0049	1.0048	1.0048
TAV$_{TB}$	18.75	18.03	18.74
M1-O1A	2.034(6)	2.031(9)	2.019(6)
M1-O1A	2.151(9)	2.098(14)	2.096(10)
M1-O2A	2.022(10)	1.982(17)	1.989(10)
M1-O1B	2.071(7)	2.051(10)	2.054(7)
M1-O1B	2.172(10)	2.129(16)	2.124(10)
M1-O2B	2.050(10)	2.040(16)	2.004(10)
<M1-O>	2.083	2.055	2.048
V$_{M1}$ (Å^3)	11.922	11.459	11.360
OQE$_{M1}$	1.0080	1.0073	1.0070
OAV$_{M1}$	24.29	22.78	21.85
M2-O1A	2.127(10)	2.108(15)	2.100(10)
M2-O2A	2.076(5)	2.080(8)	2.078(5)
M2-O3A	2.301(6)	2.264(11)	2.234(6)
M2-O1B	2.090(10)	2.080(16)	2.083(10)
M2-O2B	2.010(7)	2.002(10)	2.002(7)
M2-O3B	2.502(10)	2.401(18)	2.342(12)
<M2-O>	2.184	2.156	2.140
V$_{M2}$ (Å^3) 6 atoms	12.910	12.446	12.225
OQE$_{M2}$	1.0563	1.0525	1.0499
OAV$_{M2}$	163.87	161.58	159.28
M2-O3B	3.045(5)	3.028(8)	3.039(5)
M2-O3A	3.583(11)	3.552(18)	3.545(11)
V$_{M2}$ (Å^3) 8 atoms	22.543	21.802	21.506
O3A-O3A-O3A	161.4(4)	160.9(6)	160.3(3)
O3B-O3B-O3B	143.0(4)	141.6(5)	139.8(3)
O3A-O3B	2.923(15)	2.871(28)	2.822(15)

Notes: TQE, TAV, OQE, and OAV are quadratic elongation and angle variance for tetrahedra and octahedra (Robinson et al. 1971).

TABLE 5. Selected bond lengths (Å) and angles (°) in C2/c structure of the Di$_{15}$En$_{85}$ pyroxene, collected at P = 6.15 GPa

T-O1	1.601(5)	M1-O1A2, B2	2.021(4) ×2
T-O2	1.579(3)	M1-O1A1, B1	2.094(6) ×2
T-O3A1	1.658(8)	M1-O2C1, D1	2.006(6) ×2
T-O3A2	1.672(4)	<M1-O>	2.040
<T-O>	1.628	V$_{M1}$ (Å)^3	11.240
V$_T$ (Å)^3	2.199	TQE	1.0056
TQE	1.0046	OAV	17.90
OAV	19.79	M2-O1A1, B1	2.113(5) ×2
		M2-O2C2, B2	2.021(4) ×2
O3A2-O3A1-O3A2	137.1(2)	M2-O3C1, D1	2.265(6) ×2
O3A1-O3B1	2.820(10)	M2-O3C2, D2	3.048(4) ×2
		<M2-O>	2.364
		V$_{M2}$ (Å)^3	20.663

tween 5.3 and 7.0 GPa (Angel and Hugh-Jones 1994)] to 3.3 GPa [between 4.59 and 7.89 GPa (Ross and Reynard 1999)] by DAC experiments, or even more in measurements performed with multianvil assemblages (Shinmei et al. 1999). The differences in the extent of the hysteresis may be interpreted as related to non-hydrostatic stress and/or the lack of structural relaxation at the transition. Structural relaxation is probably lacking in the

measurement performed using synchrotron radiation and multianvil assemblage by Shinmei et al. (1999): multianvil assemblage is not hydrostatic at room temperature and the fast collection with synchrotron radiation does not warrant full relaxation. The difference in hysteresis between the studies of Angel and Hugh-Jones (1994) and Ross and Reynard (1999) may derive from the use respectively of single-crystal XRD and powder Raman spectroscopy to detect the transition. The latest technique, in fact, is probing the transition at a local scale and moreover
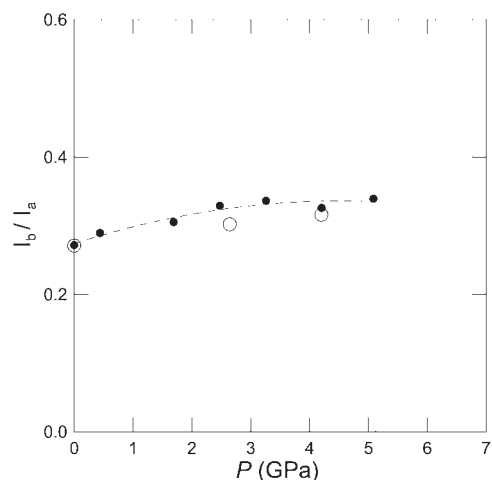
FIGURE 2. Evolution of the ratio I_b/I_a of the intensities of $h + k$ odd (b-type) and $h + k$ even (a-type) reflections with P. I_a was obtained by averaging the intensities of the $(1\ \overline{3}\ 3)$, $(1\ \overline{3}\ \overline{1})$, $(2\ 0\ 2)$, and $(0\ 6\ 2)$ reflections, I_b those of $(0\ 5\ 2)$, $(2\ \overline{3}\ \overline{1})$, $(2\ \overline{3}\ 3)$. Full dots refer to data collected at each pressure, open circles to the square of the calculated structure factors on the same reflections at the end of full structure refinements. Note that both suggest a slight increase in the intensity with pressure.

non-hydrostatic deviatoric stress may occur due to the use of powdered samples. In the present work, the same procedure described by Angel and Hugh-Jones (1994) has been used and, therefore, we do not consider the disappearance of hysteresis an artifact. It is here proposed that substitution of a small amount of Ca into the clinoenstatite structure might facilitate the nucleation of one structure from the other during the first-order transition process. A similar behavior is present in Fe-bearing pyroxenes along the join enstatite-ferrosilite (Ross and Reynard 1999); for these clinopyroxenes, the hysteresis decreases with ferrosilite content, and becomes undetectable for Fe contents higher than 50%. The effect of Ca seems stronger than that of Fe in decreasing the hystheresis.

Equation of state

The equation of state of the $P2_1/c$ and $C2/c$ phases was determined by fitting a third-order Birch-Murnaghan equation of state to the P-V data (Table 1). The fitting was performed using the EOSFIT program (Angel 2000). For the $P2_1/c$ phase, the initial volume V_0, room pressure isothermal bulk modulus K_{T0}, and its first-derivative K' have been refined simultaneously; for the $C2/c$ phase, only V_0 and K_{T0} have been refined, while K' has been kept fixed to the same value determined for the $P2_1/c$ phase (Table 6).

A visual diagnostic tool to understand the quality of an EoS fit is the F_E–f_E plot. For the Birch-Murnaghan EoS, based upon the Eulerian definition of finite strain f_E $\{(f_E = [(V_0/V)^{2/3} - 1] / 2)\}$ a "normalized stress" is defined as $F_E = P/3\ f_E\ (1 + 2\ f_E)^{5/2}$ (Angel 2000). For the $P2_1/c$ data of this work, the F_E–f_E plot (Fig. 3) shows that all data lie on an inclined straight line. From the intercept and slope of such linear fitting, we obtain $K_{T0} = 102.0$ and $K' = 8.0$, in excellent agreement with the calculated fit. This result confirms that the data are described adequately by a third-
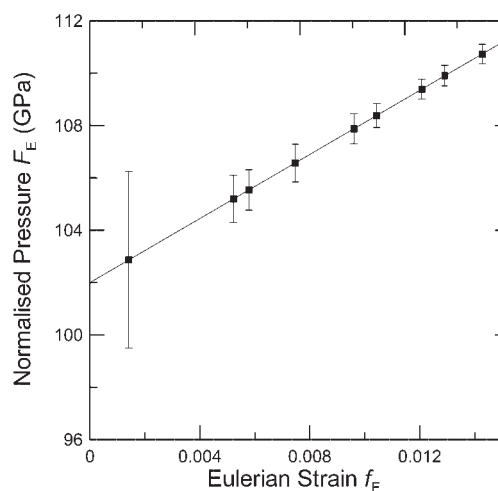

FIGURE 3. F_E-f_E plot for the equation of state of the $P2_1/c$ phase

TABLE 6. Coefficients obtained by fitting a third-order Birch-Murnaghan EoS to the unit-cell constant

	$P2_1/c$	$C2/c$
a_0 (Å)	9.6523(4)	9.4838(4)
$K_{T0, a}$ (GPa)	96(1)	79(3)
K'_a	10.7(8)	=
b_0 (Å)	8.8461(3)	8.8441(2)
$K_{T0, b}$ (GPa)	83.8(8)	98(1)
K'_b	5.9(4)	=
c_0 (Å)	5.2035(7)	5.0536(3)
K_{T0} (GPa)	98(4)	84(5)
K'_c	11(2)	=
$a\sin\beta_0$ (Å)	9.1608(5)	9.2148(4)
$K_{T0, a\sin\beta}$ (GPa)	136(4)	126(6)
$K'_{a\sin\beta}$	10(2)	=
V_0 (Å³)	421.68(8)	411.06(3)
K_{T0}(GPa)	102(2)	108(2)
K'	8(1)	=

Note: The K' values for the $C2/c$ phase are fixed to K' of the $P2_1/c$ phase.

order truncation of the Birch-Murnaghan EoS (Angel 2000).

The degree of correlation between K_{T0} and K' needs also to be assessed. In general, differences even larger than the error simply may be artifacts arising from different fitting procedures (Angel 2000). To verify the correlation degree, a confidence ellipse was constructed in the parameter space whose axes **x** and **y** represent the values K_{T0} and K'. Figure 4 shows the confidence ellipse for our $P2_1/c$ data referred to a 68.3% confidence level (2-parameter analogue of a 1σ error bar for a single parameter). The individual error bars of K_{T0} and K' also reported in the plot are smaller than the total range represented by the confidence ellipse, therefore they alone do not represent the true uncertainty of these two values.

The $P2_1/c$ phase of $Di_{15}En_{85}$ shows a decrease of K_{T0} in comparison with pure clinoenstatite (Angel and Hugh-Jones 1994), from 111.1(3.3) to 102(2) GPa. For the $C2/c$ phase the comparison is less significant, due to the limited pressure range of the data used for the $C2/c$ fit. The bulk modulus for the $C2/c$ phase [$K=108(2)$] is not different within the uncertainties of other investigations on samples with different Ca content along the join diopside-enstatite (Tribaudino et al. 2001).
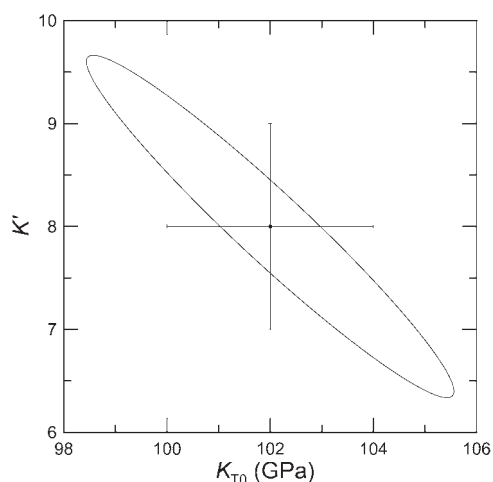
FIGURE 4. Confidence ellipse for the $P2_1/c$ equation of state

A third-order Birch-Murnaghan EoS was used to fit the evolution of the individual unit-cell parameters as a function of pressure. The cube of the lattice parameter was substituted for the volume in the EoS. To obtain the variation of β angles with pressure, the fit on $a\sin\beta$ parameter was divided by the corresponding fit of the unit-cell parameter a.

The EoS parameters are given in Table 6. The compression of the unit-cell parameters is markedly anisotropic, showing the following scheme: $\beta_b > \beta_a \cong \beta_c > \beta_{a\sin\beta}$ for both $P2_1/c$ and $C2/c$ phases. The same axial compressibility scheme was observed in clinoenstatite (Angel and Hugh Jones 1994), diopside and $Di_{80}En_{20}$ (Tribaudino et al. 2000), and looks unrelated to Ca-Mg substitution.

Structure evolution

Structural data at 0.0001, 2.6, 4.5, and 6.2 GPa were obtained for $Di_{15}En_{85}$. Good-quality refinements of $P2_1/c$ structures allow the details in the evolution of this phase to be evaluated before the transition to $C2/c$ occurs.

The compression of the M2 (based on 6 O atoms) and M1 polyhedra occur at a similar rate (linear volume compressibility between room P and 4.5 GPa is 10.5 and $11.8 \cdot 10^{-3}$/GPa for the M1 and M2 octahedra, respectively). The SiO_4 tetrahedra, as expected, do not show strong compression. The O3-O3-O3 kinking angles of A and B chains decrease, i.e., considering that the kinking occurs in an opposite sense of rotation in the two chains become more different with increasing pressure (Fig. 5); the bond distances between M2 and the six closest O atoms, i.e. those within coordination become more similar, so that the M2 polyhedral distortion decreases (Fig. 6a). However, to clarify the transition mechanism, the O3 atoms outside the coordination polyhedra (Fig. 6b) also must be considered (Downs et al. 1999). The M2 cavity in pyroxenes is surrounded by 8 O atoms, of which four are O3 bridging O atoms, two from each of the A and B chains. In Ca-rich $C2/c$ pyroxenes, four pairs of symmetry equivalent M2-O distances are present, as the eight O atoms facing in the M2 cavity are all coordinated by the relatively large cation in the M2 site. In the $P2_1/c$ structure, due to symmetry reduction, the four pairs become eight independent distances.
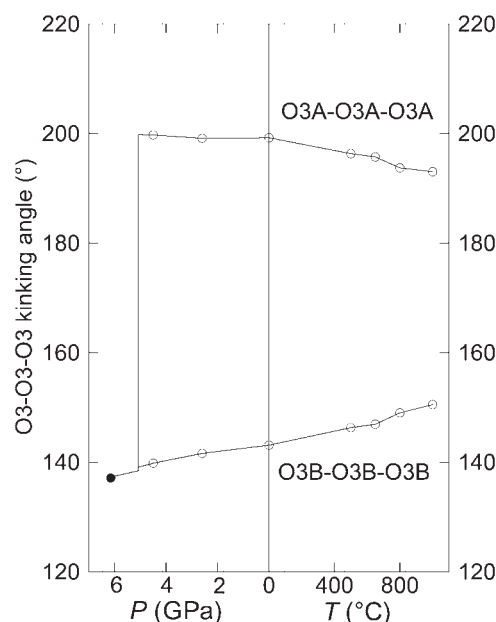

FIGURE 5. O3-O3-O3 tetrahedral chain kinking angle in the $Di_{15}En_{85}$ pyroxene with pressure and temperature in $P2_1/c$ phase (open circle, as in following figures); high pressure $C2/c$ phase (full circle, as in the following figures). Here and in the following figures: data for high and room pressure = this work; data for high temperature = Tribaudino et al. (2002). Note that the A chain is S-rotated, therefore the kinking angle is expressed as 360-(O3-O3-O3).

Substitution of a smaller cation like Mg for Ca reduces the actual M2 coordination to 6, as found in $Di_{15}En_{85}$ pyroxene. In this case, the $P \rightarrow C$ transition reduces independent bond lengths from 6 to 3. Namely, they are M2-O2A and B, M2-O1A and B, and the two shortest distances from the O3 atoms M2-O3A and O3B (Figs. 6a and 7). At room condition for $Di_{15}En_{85}$ pyroxene, two of the four O3 atoms are out of coordination, with M2-O3 distances respectively of about 3.0 (M2-O3B) and 3.5 (M2-O3A) Å (Figs. 6b and 7). At the high-pressure transition, the longest M2-O3A distance decreases by as much as 1.2 Å, it becomes equivalent to the shorter of the two M2-O3B distances, and falls into coordination (Figs. 6b and 7). In the high-temperature phase transition, it is the longer of the M2-O3B distances that falls into coordination (Fig. 6b). Examining the evolution of the $P2_1/c$ structures as a function of temperature, it appears that the difference between bond distances of M2-O3 pairs, which become equivalent in the $C2/c$ symmetry, decreases as the transition is approached, whereas an increase is observed in the high pressure behavior.

The evolution of the $P2_1/c$ structure with pressure confirms previous studies on the mechanism of the transition (Hugh-Jones et al. 1994; Downs et al. 1999). The main changes occur at the M2 polyhedron and are related to the change of the sense of rotation of the A chain, that from S-rotated becomes O-rotated in order to be equivalent to the B chain. The resulting HP-$C2/c$ structure has strongly inflected chains, and an arrangement close to a distorted cubic packing of O atoms.
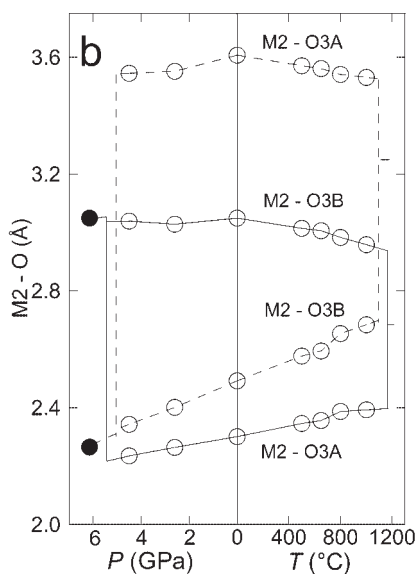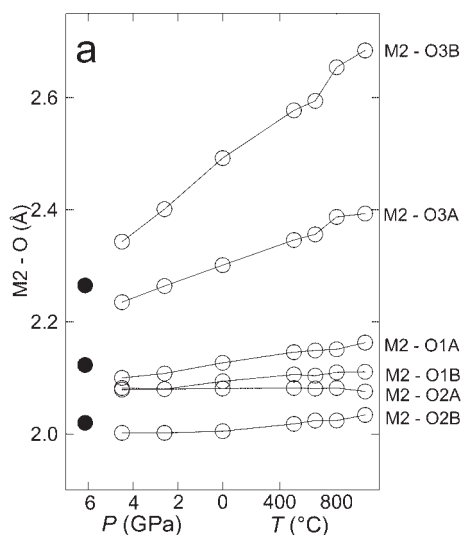
DISCUSSION

Pre-transition behavior of the $P2_1/c$ phase at high pressure and high temperature

It has been shown that the mechanisms of the high-temperature and high-pressure phase transitions are quite different. In both HP and HT structures, the tetrahedral A and B chains of the $P2_1/c$ phase become equivalent, but with different chain kinking. The HT-$C2/c$ structure has extended chains, and a distorted hexagonal packing (Thompson and Downs, in press), whereas the HP-$C2/c$ structure has kinked chains and a distorted cubic packing. Another clear difference is the behavior of the O3A and O3B atoms out of coordination of the M2 polyhedron (Fig. 6b). In the HT-$C2/c$ structure, the O3B comes closer to M2 and therefore into coordination (Downs et al. 1999), whereas in the HP-$C2/c$ phase it is the O3A that exhibit such behavior.

The structural evolution at high pressure of the $P2_1/c$ phase of sample $Di_{15}En_{85}$ can be compared with that at high temperature obtained for the same sample by Tribaudino et al. (2002).

In Figures 6a and 6b, the evolution with temperature and pressure of the M2-O distances is shown. An "opposite" behavior is visible, i.e., bond lengths expand with increasing temperature and decrease with increasing pressure. Also, the O3-O3-O3 chain kinking follows an opposite trend (Fig. 5), with A and B chains becoming more similar at high temperature. In general, the behavior can be expected for a given structure (Hazen and Finger 1982), as pressure and temperature are usually inversely related.

◄ FIGURE 6. Changes of bond lengths with pressure and temperature in $Di_{15}En_{85}$ pyroxene in $P2_1/c$ phase (open circle) and high-pressure $C2/c$ phase (full circle). (**a**) M2-O coordinated bond lengths; in the $C2/c$ phase, the distances refer to M2-O2C2, B2, to M2-O1A1, B1 and to M2-O3C1, D1, from bottom to top. (**b**) M2-O3 distances, including those out of coordination. Full and dotted lines connect pairs of bond lengths that become equivalent at the attainment of the $C2/c$ symmetry. The high-pressure and high-temperature transition pressure and temperature are different for the two pairs of O atoms the sake of clarity. The critical pressure comes from this work, the critical temperature from Landau modeling in Tribaudino et al. (2002). The high-temperature $C2/c$ bond distance was taken from Smyth (1974).
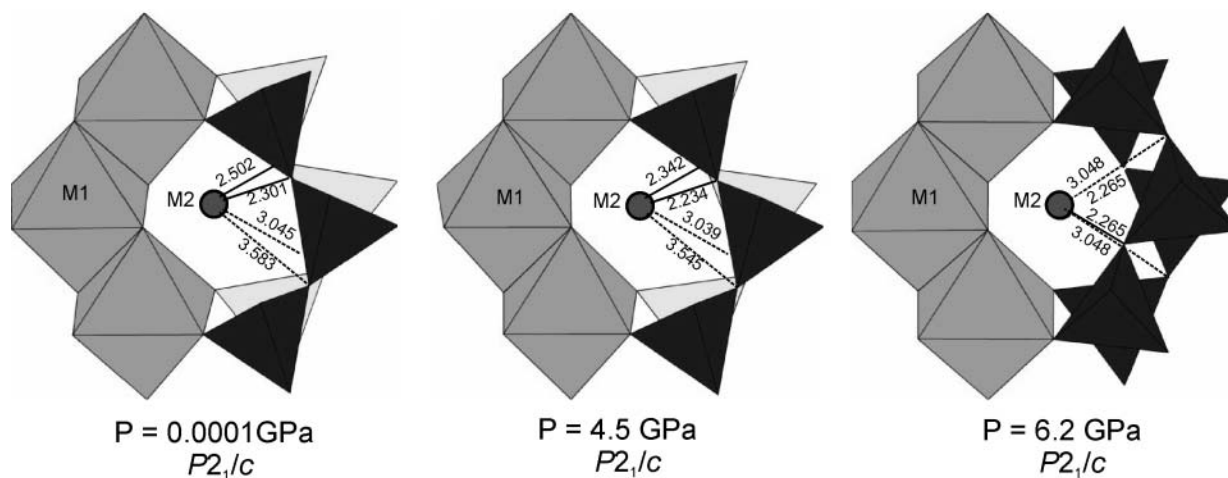

FIGURE 7. Structure drawing showing changes in the M2 coordination geometry for the two $P2_1/c$ structures at $P = 0.0001$ and 4.5 GPa and for the $C2/c$ structure at $P = 6.2$ GPa. Distances between the M2 and O3 bridging O atoms are reported (in Å); the A chain is filled, the B chain open.
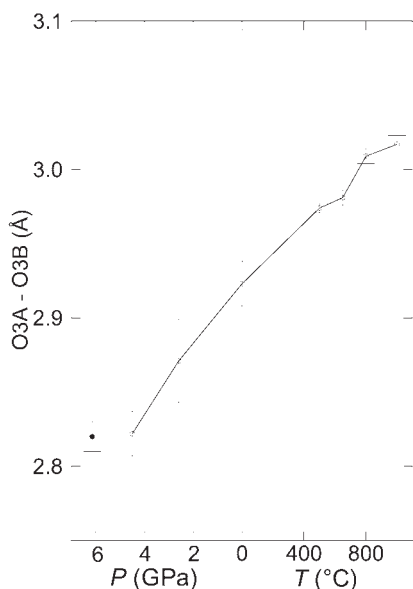
FIGURE 8. Distance between O atoms in facing tetrahedral chains (O3A-O3B) as a function of pressure and temperature.

It is this behavior that affects directly the mechanism of the phase transformation. For example, the decrease of chain kinking approaching the transition at high temperature suggests, even before the transition is achieved, a tendency toward a $C2/c$ structure with equivalent elongated chains. At high pressure, however, both chains become more kinked, with a consequent increase of their kinking difference, as the A chain is S-rotated. Thus, the transition requires an abrupt change in the sense of rotation of the A chain (Hugh-Jones et al. 1994). Such structural behavior may explain the different evolution of the intensities of $h + k$ = odd reflections. These reflections show a slight increase with pressure and a sudden drop at the transition pressure (Fig. 2). This increase may not be significant, but the general trend is surely different from the high-temperature behavior, which involves a decrease of the intensities of $h + k$ = odd reflections between room temperature and the transition. The above considerations apply to the general evolution of $P2_1/c$ pyroxenes with pressure, as an increase in the difference of the chain-kinking angles with increasing pressure was found also for $P2_1/c$ spodumene and $LiScSi_2O_6$ by Arlt and Angel (2000).

The sudden structural rearrangement of the A chains that occurs at the transition may be a result of the repulsion between the O3 atoms belonging to opposite tetrahedral chains. As shown in Figure 8 their distance increases with temperature, but decreases with pressure. The structural rearrangement at the high-pressure transition avoids a further approach that would occur due to further kinking of the two tetrahedral chains. As a result of the phase transformation, both tetrahedral chains are O-rotated in the $C2/c$ structure and the O3-O3 distance is still 2.82 Å at 6.15 GPa (Fig. 8).

Thermodynamic behavior of the HP $P2_1/c$-$C2/c$ phase transition along the join diopside-enstatite

Calcium substitution along the join En-Di causes a significant decrease of P_c, in agreement with the predictions of Arlt et al

(2000), although precise comparison is biased by large hysteresis in clinoenstatite. A critical pressure of 6.2 GPa can be estimated from the data along the join En-Fs by Ross and Reynard (1999), which corresponds to the average of the hysteresis bracket in Angel and Hugh-Jones (1994). A simple linear extrapolation between the P_c of clinoenstatite and that of the present study would predict a critical pressure of 2.8 GPa for the composition of $Di_{50}En_{50}$, which is in good agreement with the observed disappearance of the $h + k$ = odd reflections for $Di_{50}En_{50}$ (Fig. 3 in Tribaudino et al. 2001), and corresponds to the threshold beyond which the spontaneous strain related to the transition begins to decrease (Tribaudino et al. 2001). A large strain tail was observed between about 3 and 5 GPa for sample $Di_{50}En_{50}$, but was not present in clinoenstatite and in $Di_{15}En_{85}$. It should be noted that, in the powder XRD experiment with $Di_{50}En_{50}$, the pressure was increased and decreased at a rather fast rate, but no hysteresis was observed.

The transition character is first order for both clinoenstatite and $Di_{15}En_{85}$, whereas for higher Ca content [e.g., $Di_{50}En_{50}$ (Tribaudino et al. 2001)], the transition seems to become continuous. A different transition mechanism may therefore be present in intermediate clinopyroxenes. A change from first-order to continuous transformation behavior for clinopyroxenes with high Ca content was also observed as a function of temperature for compositions between $Di_{40}En_{60}$ and $Di_{59}En_{41}$ (Tribaudino et al. 2003). For these samples, a model involving growth of the $C2/c$ phase pinned by local compositional inhomogeneities was proposed: in compositionally heterogeneous samples, the transition is reached at a different T in different parts of the crystal. As a result, at a given T a diffraction pattern averaging coexisting $P2_1/c$ and $C2/c$ phases can be obtained, and unit-cell parameters of intermediate values between pure $C2/c$ and $P2_1/c$ phases are observed. The transition therefore looks continuous at a mesoscopic scale, although at a local microscopic scale, the structural changes may still occur by a first-order mechanism. In samples with homogeneous compositions and large antiphase domains, like $Di_{15}En_{85}$, the transition occurs at a given temperature for the whole crystal. The model proposed for high temperature follows the TEM observations of Shimobayashi and Kitamura (1991) that proposed a diffusionless athermal martensitic model for the transition. In that model, the actual transformed volume depends on the temperature, i.e., T/Tc, rather than upon time at constant temperature. It is proposed here that the same model holds for high pressure at room temperature. In the high-pressure case, the applied stress is the driving force and the austenite is the $P2_1/c$ phase, which is the martensite in the high-temperature transition. The growth of the domains is related to the elastic energy inherent in the transition rather than on temperature, and thus also can occur at room P. The continuous change of the transformed volume with pressure at the microscopic scale would then account for a continuous behavior in the compositionally heterogeneous $Di_{50}En_{50}$ clinopyroxene (as shown by TEM in Tribaudino 2000), whereas the transition may be locally first order. Similarly in $Di_{15}En_{85}$ and enstatite, which are compositionally homogeneous, the transition occurs at a given pressure for the whole crystal.

REFERENCES CITED

Allan, D.R., Miletich, R., and Angel, R.J. (1996) A diamond-anvil cell for single crystal X-ray diffraction studies to pressures in excess of 10 GPa. Review of Scientific Instruments, 67, 840–842.

Angel, R.J. (2000) Equations of state. In R.M. Hazen and R.T. Downs, Eds., Reviews in Mineralogy: High temperature and high pressure crystal chemistry, 41, 117–211. Mineralogical Society of America, Washington, D.C.

Angel, R.J. (2003) Automated profile analysis for single-crystal diffraction data. Journal of Applied Crystallography, 36, 295–300.

Angel, R.J., and Hugh-Jones, D.A. (1994) Equations of state and thermodynamic properties of enstatite pyroxenes. Journal of Geophysical Research, 99, 19777–19783.

Angel, R.J., Chopelas, A., and Ross, N.L. (1992) Stability of high –density clinoenstatite at upper mantle pressures. Nature, 358, 322–324.

Angel, R.J., Allan, D.R., Miletich, R., and Finger, L.W. (1997) The use of quartz as an internal pressure standard in high pressure crystallography. Journal of Applied Crystallography, 30, 461–466.

Angel, R.J., Downs, R. T., and Finger, L.W. (2000) High-temperature–high-pressure diffractometry. In R.M. Hazen and R.T. Downs, Eds., High temperature and high pressure crystal chemistry, 41, 559–596. Reviews in Mineralogy, Mineralogical Society of America, Washington, D.C.

Arlt, T. and Angel, R.J. (2000) Displacive phase transitions in C-centered clinopyroxenes: spodumene, $LiScSi_2O_6$ and $ZnSiO_3$. Physics and Chemistry of Minerals, 27, 719–731.

Arlt, T., Angel, R.J., Miletich, R., Armbruster, T., and Peters, T. (1998) High pressure $P2_1/c$-$C2/c$ phase transitions in clinopyroxenes: influence of cation size and electronic structure. American Mineralogist, 83, 1176–1181.

Arlt, T., Kunz, M., Stoltz, J., Armbruster, T., and Angel, R.J. (2000) P-T-X data on $P2_1/c$ clinopyroxenes and their displacive phase transitions. Contributions to Mineralogy and Petrology, 138, 35–45.

Bozhilov, K.N., Green II, H.W., and Dobrzhinetskaya, L. (1999) Clinoenstatite in Alpe Arami peridotite: additional evidence of very high pressure. Science, 284, 128–132.

Bruno, E., Carbonin, S., and Molin, G.M. (1982) Crystal structure of Ca-rich clinopyroxenes on the $CaMgSi_2O_6$-$Mg_2Si_2O_6$ join. Tschermaks Mineralogische und Petrographische Mitteilungen, 29, 223–240.

Burnham, C.W., Clark, J.R., Papike, J.J., and Prewitt, C.T. (1967) A proposed crystallographic nomenclature for clinopyroxene structure. Zeitschrift für Kristallographie, 125, 109–119.

Downs, R.T., Gibbs, G.V., and Boisen, M.B. (1999) Topological analysis of the $P2_1/c$ to $C2/c$ transition in pyroxenes as a function of temperature and pressure. AGU fall meeting, V31C-10.

Hazen, R.M. and Finger, L.W. (1982) Comparative Crystal Chemistry, 231 p. Wiley, Chichester.

Hugh-Jones, D.A., Woodland, A.B., and Angel, R.J. (1994) The structure of high pressure $C2/c$ ferrosilite and crystal chemistry of high-pressure $C2/c$ pyroxenes. American Mineralogist, 79, 1032–1041.

King, H.E. and Finger, L.W. (1979) Diffracted beam crystal centering and its application to high-pressure crystallography. Journal of Applied Crystallography, 12, 374–378.

Pasqual, D., Molin, G., and Tribaudino, M. (2000) Single-crystal thermometric calibration of Fe-Mg order-disorder in pigeonites. American Mineralogist, 85, 953–962.

Ralph, R.L. and Finger, L.W. (1982) A computer program for refinement of crystal orientation matrix and lattice constraints from diffractometer data with lattice symmetry constraints. Journal of Applied Crystallography, 15, 537–539.

Robinson, K., Gibbs, G.V., and Ribbe, P.H. (1971) Quadratic elongation; a quantitative measure of distortion in coordination polyhedra. Science, 172, 567–570.

Ross, N.L. and Reynard, B. (1999) The effect of iron on the $P2_1/c$ to $C2/c$ transition in $(Mg,Fe)SiO_3$ clinopyroxenes. European Journal of Mineralogy, 11, 585–589.

Ross, N.L. and Sowerby, J. R. (1999) High Pressure Crystal Field Spectra of Single Crystal Clinoferrosilite. European Journal of Mineralogy, 11, 791–801.

Sheldrick, G.M. (1997) Programs for Crystal Structure Analysis (Release 97-2). Institüt für Anorganische Chemie der Universität, Tammanstrasse 4, D-3400 Göttingen, Germany, 1998.

Shimobayashi, N. and Kitamura, M. (1991) Phase transition in Ca-poor clinopyroxenes: a high temperature transmission electron microscopic study. Physics and Chemistry of Minerals, 18, 153–160.

Shinmei, T., Tomioka, N., Fujino, K., Kuroda, K., and Irifune, T. (1999) In situ X-ray diffraction study of enstatite up to 12 GPa and 1473 K and equations of state. American Mineralogist, 84, 1588–1594.

Smyth, J.R. (1974) The high temperature crystal chemistry of clinohypersthene. American Mineralogist, 59, 1061–1082.

Tribaudino, M. (2000) A transmission electron microscope investigation on the $C2/c$ -$P2_1/c$ phase transition in clinopyroxenes along the diopside-enstatite $(CaMgSi_2O_6$-$Mg_2Si_2O_6)$ join. American Mineralogist, 85, 707–715.

Tribaudino, M. and Nestola, F. (2002) Average and local structure in $P2_1/c$ clinopyroxenes along the join diopside-enstatite $(CaMgSi_2O_6$-$Mg_2Si_2O_6)$. European Journal of Mineralogy, 14, 549–555.

Tribaudino, M., Prencipe, M., Bruno, M., and Levy, D. (2000) High pressure behaviour of Ca-rich $C2/c$ clinopyroxenes along the join diopside-enstatite $(CaMgSi_2O_6$-$Mg_2Si_2O_6)$. Physics and Chemistry of Minerals, 27, 656–664.

Tribaudino, M., Prencipe, M., Nestola, F., and Hanfland, M. (2001) A $P2_1/c$-$C2/c$ high pressure phase transition in $Ca_{0.5}Mg_{1.5}Si_2O_6$ clinopyroxene. American Mineralogist, 86, 807–813.

Tribaudino, M., Nestola, F., Cámara, F., and Domeneghetti, M.C. (2002) The high temperature $P2_1/c$-$C2/c$ phase transition in Fe-free pyroxenes: structural and thermodynamic behavior. American Mineralogist, 87, 648–657.

Tribaudino M., Nestola F., Meneghini C. and Bromiley G.D. (2003) The high temperature $P2_1/c$-$C2/c$ phase transition in Fe-free Ca-rich $P2_1/c$ clinopyroxenes. Physics and Chemistry of Minerals, 30, 527–535.

Wilson, A.J.C. Editor (1995) International Tables for Crystallography, Volume C. Kluwer Academic Publishers, Dordrecht, The Netherlands.